






RESEARCH ARTICLE | JULY 06 2023

Experimental analysis of a propeller noise in turbulent flow

Nur Syafiqah Jamaluddin ; Alper Celik ; Kabilan Baskaran ; Djamel Rezgui ; Mahdi Azarpeyvand 



Physics of Fluids 35, 075106 (2023)

<https://doi.org/10.1063/5.0153326>



CrossMark

Articles You May Be Interested In

Numerical study of rotor unsteady forces and noise due to ingestion of grid-generated turbulence

Physics of Fluids (January 2023)

Acoustics of rotor ingesting an axisymmetric turbulent boundary layer

J Acoust Soc Am (October 2021)

Haystack radio telescope

Physics Today (January 1965)

Experimental analysis of a propeller noise in turbulent flow

Cite as: Phys. Fluids **35**, 075106 (2023); doi: [10.1063/5.0153326](https://doi.org/10.1063/5.0153326)

Submitted: 6 April 2023 · Accepted: 14 June 2023 ·

Published Online: 6 July 2023



View Online



Export Citation



CrossMark

Nur Syafiqah Jamaluddin,^{1,a)}  Alper Celik,^{1,2,b)}  Kabilan Baskaran,^{1,3,c)}  Djamel Rezgui,^{1,d)} 
and Mahdi Azarpeyvand^{1,e)} 

AFFILIATIONS

¹Department of Aerospace Engineering, University of Bristol, Bristol BS8 1TH, United Kingdom

²Department of Aerospace Engineering, Swansea University, Swansea SA1 8EN, United Kingdom

³Department of Mechanical Engineering, Indian Institute of Technology, Dhanbad 826004, India

^{a)} Author to whom correspondence should be addressed: syafiqah.jamaluddin@bristol.ac.uk

^{b)} Electronic mail: alper.celik@swansea.ac.uk

^{c)} Electronic mail: kabilan@iitism.ac.in

^{d)} Electronic mail: djamel.rezgui@bristol.ac.uk

^{e)} Electronic mail: m.azarpeyvand@bristol.ac.uk

ABSTRACT

This paper presents a comprehensive experimental aeroacoustic investigation of a propeller under turbulence ingestion. Two turbulence-generating passive grids were utilized to quantify the effect of turbulence intensity on the aeroacoustic characteristics of the propeller. A two-component hot-wire anemometry was employed to study the flow field. The flow field results demonstrate a substantial increase in fluctuating velocity components in both axial and radial directions, concentrated at the mid-span of the blade and near the tip, respectively. Energy spectral analysis in the vicinity of the propeller blade shows significantly higher broadband energy levels with multiple haystacking peaks at the harmonics of the blade passage frequency. Far-field noise and load measurement results show that turbulence ingestion has a strong effect on the aerodynamic loading and acoustic response at the blade passage frequency. The directivity of noise radiation at low frequency shows a significant tonal noise contribution. Meanwhile, broadband noise radiation is more dominant at a higher range of frequency, especially when the propeller is operated with turbulence ingestion and at higher advance ratio settings. The far-field noise results revealed the haystacking trends in the low frequency domain of the spectra and are most significant for propellers operating in turbulent inflows.

© 2023 Author(s). All article content, except where otherwise noted, is licensed under a Creative Commons Attribution (CC BY) license (<http://creativecommons.org/licenses/by/4.0/>). <https://doi.org/10.1063/5.0153326>

I. INTRODUCTION

The electric propeller-driven air transport system is one of the novel solutions for future urban transportation of goods and people. Propellers or rotors are vital components used to power air mobility technologies.¹ Over 300 electrically powered vertical takeoff and landing (eVTOL) prototypes have been proposed, primarily conceptualized using propeller blades. The Vertical Flight Society maintains a World eVTOL Aircraft Directory database.² The use of propellers in the new generation of urban air vehicles offers many potential benefits, including the efficiency of low-speed rotary wings and the vectored-thrust maneuverability that allows vertical takeoff and landing operations. Despite the wide range of applications, noise is an important consideration for urban air mobility (UAM) as it is anticipated to operate in communities close to the public.

Propeller acoustic sources emit high-intensity tonal and broadband noise, which is particularly unpleasant for humans. This propeller-associated noise pollution remains a feasibility barrier to the technology, and therefore, propeller acoustics and low-noise control continue to be inevitable scientific research areas.³ The rotary-wing-driven system exhibits relatively complex sound-generating mechanisms. Propellers propagate sound spectra that are rich in tonal and broadband content to the far-field. The tonal noise is predominantly associated with the blade loading condition and blade geometry, which correspond to the volume displacement effects.⁴⁻⁶ Meanwhile, the broadband noise sources are mainly due to turbulence ingestion at the blade leading edge and turbulent boundary-layer trailing-edge noise.⁷ Experimental studies conducted by Pettingill *et al.*⁸ showed that the generation of broadband noise is highly dependent on the transition of

the boundary layer along the blade surface, with additional secondary effects due to tip vortex generation. Moreover, at any given operation setting, propellers generate noise through various mechanisms, each contributing to the overall noise at different levels and strengths. Understanding the contribution of tonal and broadband noise in the acoustic spectrum of rotating blades is important. Previous studies have shown that propeller noise can be decomposed into tonal and broadband components by using wavelet technique.^{9,10}

The noise emission levels from a propeller can be significantly influenced by its kinematics and operating parameters, such as the rotational speed, inflow velocity, inflow angle, and inflow turbulence. These factors become particularly crucial during cruising, primarily due to the strong blade vortex interactions that the blade experience under forward flight conditions.^{11,12} Depending on these parameters, each blade section may experience variations in both the magnitude and direction of the velocity with each rotation, consequently influencing the overall aerodynamic interactions of the propeller.¹³ The local velocity at each blade section is a critical factor that influences both the loading and noise characteristics of the blade. A study by Jiang *et al.*¹⁴ examined the variation in blade sections of high-efficiency and low-noise propellers. Their finding revealed that the broadband noise generated by the propellers is influenced by conditions at the blade section, which includes the occurrence of flow separation at the blade trailing edges and the flow uniformity at blade tips on both suction and pressure sides. Many of recent experimental investigations used commercial off-the-shelf propeller blades, mainly due to the product readiness and availability. Wu *et al.*¹⁵ experimentally show that manufacturing uncertainty does not have a significant effect on the aeroacoustics of the propellers.

Turbulent flow ingestion is omnipresent in rotating device applications and corresponds to phenomena such as distorted atmospheric turbulence, propeller slipstream, and wing or fuselage installation effects. This phenomenon yields additional noise sources, namely, turbulence ingestion noise, which transpires each time the turbulent inflow impinges on the surface of the rotating propeller blade. The noise spectra generated by propellers operating under vortex shedding or inflow turbulence include a strong contribution of broadband components.¹⁶ The broadband noise presents as dipole sound aligned to the propeller rotational axis.^{17,18} Turbulence ingestion introduces pressure fluctuations at the leading edge of the blade, causing turbulent boundary layers to develop over most parts of the blade surface, producing sound waves as the turbulence travels over the trailing edge.¹⁹ Turbulence flow can be characterized by its characteristic length scale, timescale, intensities, and spectral content. Among these parameters, the impact of increasing turbulence intensity has been found to increase the broadband noise levels when ingested by propellers.²⁰

One of the earlier studies on the sound radiation of a rotating blade exposed to turbulence ingestion was conducted by Sevik in 1974, where a ten-bladed propeller was experimentally investigated with turbulence in the approach stream.²¹ The study determined that the intensity of radiated sound depends on the characteristic timescale of the turbulence inflow, identified as the primary contributor to broadband sound. While the study takes an interesting approach by measuring the loading and using theoretical mathematics to estimate the radiated sound, it leaves a gap in the direct acoustic measurements. Wojno *et al.*^{22,23} later addressed this by measuring the acoustic response of the same propeller under turbulence inflow. In their study,

it has been demonstrated that propeller noise radiation to the far-field can be mathematically expressed using the acoustic propagation law, which models the amplitude of sound pressure at any point in the far-field as a function of the amplitude of the unsteady thrust spectrum. Most recently, Wu *et al.* also analyzed the loading and noise generated by a ten-bladed propeller when ingesting turbulence.²⁴ Their findings suggest that turbulence ingestion introduces pressure perturbations on the propeller blades, leading to increased amplitudes of the generated unsteady thrust. The study also highlighted the strong correlation between the propeller's interaction with grid-generated turbulence by the multiple cutting of the coherent turbulent structures by the blade surfaces during each rotation.

This study aims to experimentally characterize a propeller's aeroacoustic response when subjected to homogeneous turbulence ingestion. The paper compares experimental results on the noise characteristics of propellers operating in a laminar and turbulent inflow. The laminar inflow case refers to the wind tunnel's default flow quality as detailed by Mayer *et al.*²⁵ The measurements are also performed under grid-generated turbulent inflows to address the effects of turbulence ingestion and the variations in the turbulent structure sizes. The effects of the freestream velocity are also addressed. This paper is organized as follows: Sec. II explains the experimental setup and the rig and measurement techniques used; Sec. III provides the results and discussions from the experiments conducted; and finally, Sec. IV reports the conclusion of this manuscript.

II. EXPERIMENTAL SETUP

A series of wind tunnel tests were conducted in an anechoic chamber on a two-bladed propeller that operates under axial inflow conditions with and without turbulent structures. The experiments were performed in the aeroacoustics facility of the University of Bristol, an open jet, temperature-controlled close-circuit anechoic wind tunnel. The contraction nozzle exit is 0.5 m in width and 0.775 m in height, allowing a steady operation from 5 to 40 m/s with an average turbulence intensity level of less than 0.2%. The anechoic chamber is 7.9 m long, 5.0 m wide, and 4.6 m high, with acoustically treated interiors that achieves approximately 160 Hz of cutoff frequency. For a more detailed description of the facility, the reader is referred to Mayer *et al.*²⁵

The acoustic data were collected using 23-element of 1/4-in.-diameter GRAS model 40PL microphones with an upper limit of 142 dB and a frequency range between 10 Hz and 20 kHz. These microphones were installed on a far-field polar arc, allowing noise measurement of polar angles between 40° and 150° at a distance of 1.65 m from the propeller rotation axis. A National Instruments PXIe-1082 data acquisition system was used to acquire far-field noise data. Matlab R2016a was used to program the interface between the data acquisition system and the microphones. Far-field noise measurements were collected for 16 s with a sampling rate of 2¹⁶ Hz. The aerodynamic loading data (i.e., thrust and torque) were collected using an ATI Mini40E 6-axis load cell. The load cell transducer was calibrated by the manufacturer to give a measurement uncertainty with a 95% confidence level. The load measurements were performed for a duration of 16 s and at a sampling rate of 2¹⁵ Hz.

The flow field characteristics in the upstream domain were investigated using the constant temperature anemometry (CTA) measurement technique, where the velocity components of the incoming

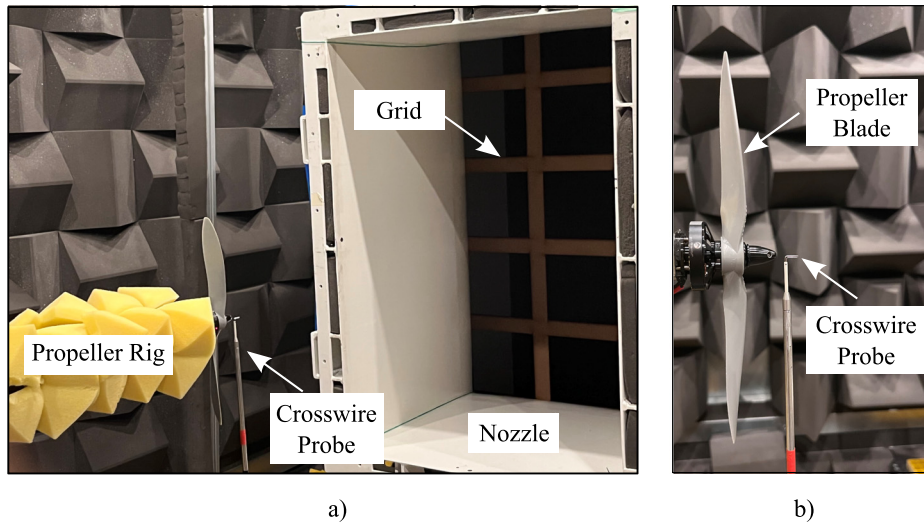


FIG. 1. Pictures of (a) the constant temperature anemometry (CTA) measurement setup, propeller rig, and grid inside the contraction and (b) the origin location of the cross-wire probe.

airflow were measured. A two-component 55P51 cross hot-wire probe was used for data acquisition on a Dantec Streamline Pro system with a CTA91C10 module and a National Instruments PXIe-4499 module. The data were sampled for 16 s at a rate of 2^{16} Hz to ensure statistical convergence in the computation of the power spectral density of the inflow velocity fluctuations. The cross-wire probes were calibrated for yaw angles between -40° and 40° using a Dantec 54H10 calibrator. The uncertainty of the measured velocity signals was found to be within $\pm 2\%$ for a freestream velocity of 20 m/s, which was determined using the procedure detailed by Jørgensen.²⁶ The probes were located at the center of the blade ($y=0$) and were initially positioned at an axial position of $x = 0.27R$, as shown in Fig. 1(b). The orientation of the cross-wire was aligned to the x -axis to measure the individual axial (U) and vertical (V) velocity components. The probe was set to traverse along the x -axis between $0.27R < x < 2.00R$ to evaluate the downstream evolution of the turbulence flow statistics. The noise, loading, and flow measurements were collected at a constant propeller rotation speed of 5000 rpm and at varying freestream inflow velocities (U_∞), corresponding to an advance ratio range between 0.47 and 0.86. The advance ratio (J) is calculated as $J = U_\infty/nD$, where D is the propeller diameter, and n is the propeller's rotational speed in revolutions per second.

The details of the test rig and instrumentation, as well as the characteristics of the grid turbulence used in the experiment, are explained in Secs. II A and II B, respectively.

A. Test rig and instruments

The current study constructed an isolated propeller test rig subjected to axial inflow conditions. Although not presented in the paper, the structure's vibration was assessed, and the results demonstrate a very low natural frequency that will unlikely resonate with the propeller when in operation. The propeller is positioned in the middle of the open jet nozzle, approximately 600 mm downstream of the nozzle exit. An off-the-shelf two-bladed propeller was used in the test, driven by a T-Motor Antigravity MN4006 brushless motor. The motor has a diameter of 44.35 mm and a maximum power of 420 W. The motor

speed was controlled by a Robotbird 100 A pro electronic speed controller. The system was powered by a DC bench power supply, which is regulated up to a maximum voltage of 25 V. Electrical current was measured at the power supply as the throttle setting of the ESC varied, which in turn changed the speed of the motor. The propeller rotation speed was determined by detecting the electrical pulse signal from one of the three wires of the brushless DC motor, taking into account the 24 poles of the motor used. The propeller speed was also inspected with a digital optical laser tachometer DT-2234C+. Figure 2 presents the schematic of the test setup in the wind tunnel with the contraction

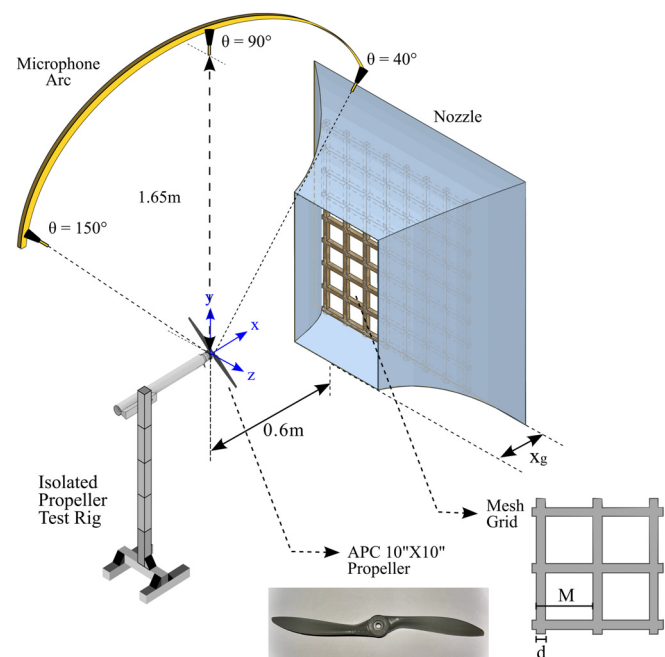


FIG. 2. Schematic diagram of the contraction nozzle with turbulence grid in position, the isolated propeller test rig, and the definition of grid dimension.

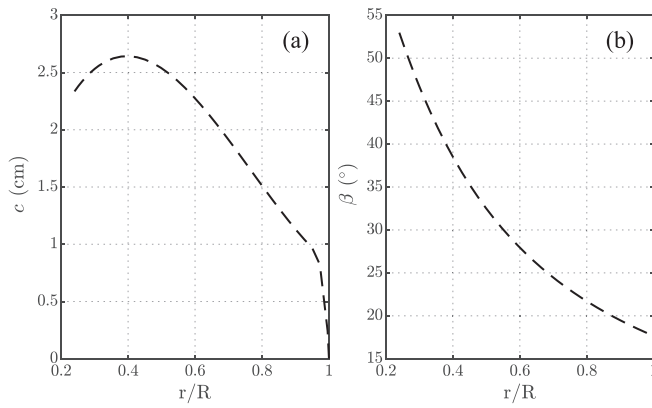


FIG. 3. Distribution of (a) the blade elemental chord length and (b) the elemental twist angle for an APC 10 × 10 propeller.

nozzle and the turbulence grid in place, the isolated propeller test rig, as well as the definition of the propeller and grid used in the present work. A Cartesian co-ordinate system (x, y, and z) is located at the hub of the propeller to ease the interpretation of the results.

A 10 × 10 APC propeller is used in the present study, which has a radius and geometric pitch of 25.4 cm, resulting in a blade pitch ratio of one. The cross sectional shape of the blade is primarily defined following the NACA 4412 and Clark-Y airfoils, except with a relatively low leading edge and thicker aft region.²⁷ Figure 3 presents the geometrical characteristics of the tested blade in terms of its chord and twist distribution over the blade’s radius. Both the chord length (c) and the twist angle (β) are most prominent near the hub of the blade, which is at around 40% and 25% of radius, respectively, and gradually reduces toward the tip.

Figure 4(a) shows the radial distribution of the estimated elemental angle of incidence (α), from the blade root (r/R = 0) to the blade tip (r/R = 1), at varying advance ratio operations. The local angle of attack near the blade’s hub, between 30% and 40% of the radius, shows relatively higher values than the rest of the blade’s sections. There are also notable differences between the angle of attack distribution at every blade element and the propeller’s advance ratio. For a constant rotational speed operation, the freestream velocity is the main factor contributing to this condition and can be mathematically expressed as follows:

$$\alpha = \tan^{-1} \frac{P}{2\pi r} - \tan^{-1} \frac{U_\infty}{2\pi n r}, \quad (1)$$

where P is the geometrical pitch of the propeller and r is the radius of the blade section. The calculation does not consider the contribution of the induced velocity, which is relatively low than the incoming flow speed. Based on this formulation, the relative inflow seen at every blade section is influenced by the value of the advance ratio, which is inversely proportional to the blade’s angle of attack. The results conform to this relationship, as the highest angle of attack values occurs at the lowest advance ratio (J = 0.47) and reduces to almost zero at J = 0.85 before turning to negative values at J = 0.94.

B. Grid turbulence characteristic

In the present study, turbulent inflows were generated by passive turbulence grids positioned inside the contraction nozzle of the facility.

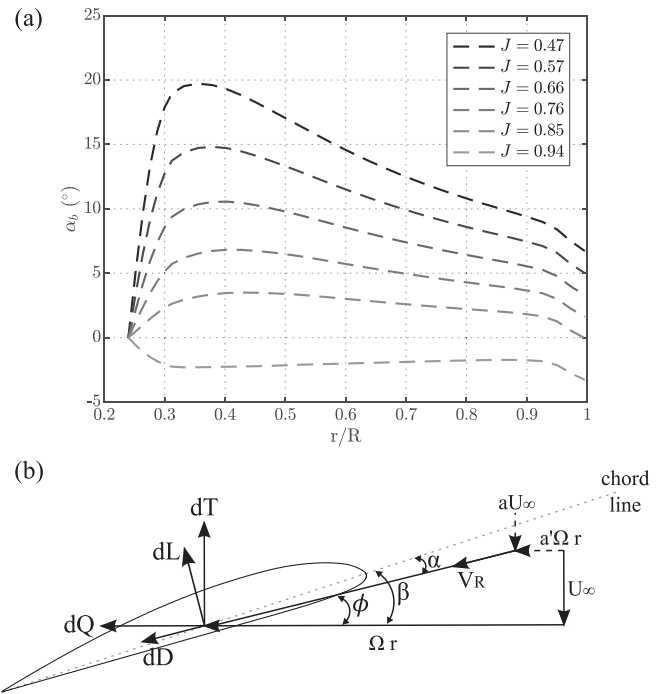


FIG. 4. Blade elemental information on (a) the distribution of the angle of incidence and (b) the force and velocity diagram.

Two types of grids, namely, grid A and grid B, were used to generate a homogeneous and near-isotropic turbulent jet stream with different turbulence levels. The grids were manufactured from MDF sheets laser cut with a Trotec SP500 CO2 laser engraver and was positioned at $x_g = 1.040$ m from the outlet of the nozzle, corresponding to a contraction ratio of 4.4. The contraction ratio (C) is calculated as the ratio of the grid to the nozzle outlet’s area, that is, $C = (A_{Grid}) / (A_{Nozzle})$. The grid measured 1.305 m in both width and height. Grids A and B differ in geometric properties such as the mesh size (M) and bar diameter (d), resulting in almost double the amount of turbulence intensity for grid B relative to grid A.

Initial tests were made to determine the nominal turbulence characteristics of each grid by Bowen *et al.*²⁸ and are briefly described below. These tests were performed for each turbulence generation grid at a freestream velocity of 20 m/s. The mean and fluctuating axial velocity data were measured using a hot-wire anemometer. The initial data were collected using a single-sensor probe, mounted normal to the freestream direction. In addition to the mean and fluctuating velocity components, the auto-spectrum and auto-correlation of the turbulence fluctuation were measured. The root mean square (rms) of the turbulence intensity and the integral scale length of the turbulence flow structure was estimated from these. The results presented in Fig. 5 indicate a near-isotropic flow characteristic for the grid-generated turbulence due to the good curve fittings between the power spectral density of velocity fluctuations for the tested grids and the Von Kármán spectrum. The geometrical properties of the grid structures in terms of diameter (d), mesh (M), and solidity (σ) are tabulated in Table I. The properties of turbulent flow generated by the grids

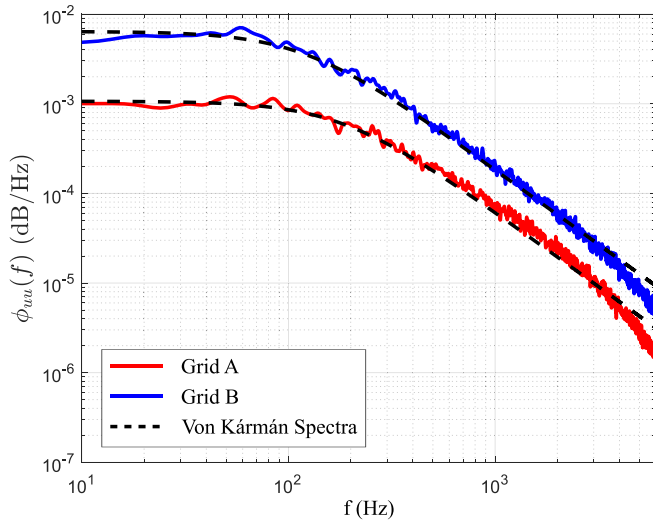


FIG. 5. The comparison of the turbulent flow characteristics measured at the exit of the contraction nozzle with the Von Kármán spectrum for near-isotropic turbulence. Reprinted with permission from Bowen *et al.*, *AIAA J.* **60**, 1833–1815 (2022). Copyright 2022 American Institute of Aeronautics and Astronautics.

TABLE I. The geometrical and turbulent flow properties generated by the corresponding grid measured at the nozzle in the wind tunnel.

	d (mm)	M (mm)	σ	TI (%)	λ (mm)
Grid A	19	100	0.35	4.9	13
Grid B	45	233	0.35	10.1	19

measured at the nozzle exit are also presented, including the turbulent intensity (TI) and length scale (λ).

III. RESULTS AND DISCUSSION

A. Aerodynamic performance of propeller in turbulence

The aerodynamic characteristics of the propeller blade are analyzed and presented in this section. A basic but fundamental

understanding of the problem can be gained by studying the aerodynamic forces acting on the blade due to the propeller action. The velocity and force diagram acting on a blade section are presented in Fig. 4(b), where the resulting force that impinges on blade surfaces comprises the axial and tangential contribution of the inflow. As the blade element momentum theory suggests, the presence of additional axial (a) and tangential inflow factor (a') induces a change in the inflow velocity in both axial and radial directions. As a result, the induced velocity flow slightly increases the axial velocity components while reducing the tangential velocity component. This change in inflow velocities causes changes in the angular characteristics of the blade section. The angle of attack of the blade section (α) reduces and, consequently, reduces the elemental thrust (dT) and torque (dQ) forces generated on the blade section.

The integration of aerodynamic forces on each blade element over the radius of the blade represents the blade’s loading that is measurable along the blade’s rotation axis. In the context of this work, this will be termed as the “hub loading.” The hub loading comprises the thrust (T) force acting normal to the plane of rotation and the angular force torque (Q). Results are presented in terms of the coefficient of thrust (C_T), coefficient of power (C_P), and efficiency (η), which are calculated as follows:

$$C_T = \frac{T}{\rho n^2 D^4}, \quad (2)$$

$$C_P = \frac{2\pi\Omega Q}{\rho n^3 D^5}, \quad (3)$$

$$\eta = J \frac{C_T}{C_P}, \quad (4)$$

where Ω is the propeller’s rotational speed in rad/s, and ρ is the air density. The aerodynamic coefficients calculated from the measurement of the tested propeller are presented in Fig. 6 in terms of the advance ratio at a constant rotational speed of 5000 rpm. Regardless of the inflow condition, the results indicate higher values of both thrust and power coefficients at a lower range of advance ratio, between $J = 0.5$ and 0.6 , while decreases at the higher ranges. At higher ranges of advance ratio, the blade experiences a reduction in its elemental angle of attack, which ultimately, in return, reduces the aerodynamic forces. The thrust and torque forces are the blade’s lift and drag derivatives, while torque is directly proportional to power. On the other

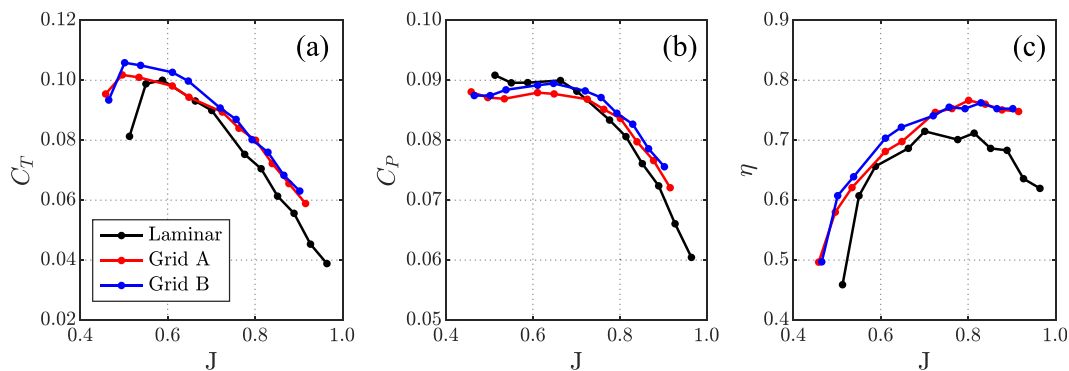


FIG. 6. The measured aerodynamic coefficients: (a) thrust coefficient, (b) power coefficient, and (c) efficiency, presented against the advance ratio for a constant rotational speed of 5000 rpm.

hand, propeller efficiency increased with advance ratio before reaching a plateau around the higher J ranges and then started declining. For instance, the laminar case, which is depicted as solid black lines, reaches its peak performance (η) at around $J=0.7$ and then reduces from approximately $J=0.8$.

When operated in grids A and B turbulent inflows, the propeller demonstrates a slight increase in thrust, power, and efficiency at the same operational setting as in laminar inflow, as depicted by the solid red and blue lines, respectively. When comparing the laminar and grid turbulence cases, the results indicate an approximately 5%–10% increase in thrust and power coefficients, albeit, when both grid turbulence cases are evaluated next to each other, the results are comparable. This trend is prevalent in most advance ratio settings, especially at an advance ratio higher than 0.6. These results suggest that more power is required to rotate the propeller through extraneous turbulence compared to when operated under laminar inflow. Due to the pressure drop induced by the inflow distortion, ingesting the grid turbulence influences the blade loadings, forcing the propeller to generate a more significant pressure increase to compensate for the differences. As discussed later, this will also influence the noise generated by the blade, as it operates in drastically different conditions.

Notably, ingesting grid turbulence inflows also increases the propeller efficiency over a more extensive range of advance ratios, which is consistent with the literature. Previous studies by Dominique *et al.* have shown that introducing non-uniform inflows strongly affects the static pressure difference between the upstream and downstream pressure sections when studying a rotating fan in distorted inflow generated by mesh grids in a wind tunnel facility.²⁹ A higher pressure rise is demonstrated under distorted inflow, leading to an increase in the aerodynamic efficiency of up to 8%. At an advance ratio of 0.8, the propeller's peak performance (η) in laminar inflow is roughly 70%, while in both grid inflows, the peak performance increases to approximately 76%.

B. Mean and fluctuating velocity fields upstream of rotation plane

Flow field analysis was conducted to investigate the flow perturbation within the upstream flow domain due to the propeller's motion and turbulence ingestion. Two-point velocity measurements were performed using a calibrated cross-wire probe. The hot-wire anemometry measurements were performed at a Reynolds number of 1.14×10^4 based on the chord length at a 75% span location of the propeller blade, corresponding to the flow velocity of $U_\infty = 10$ m/s. The digitization of the hot-wire signal yields an N statistically independent sample distribution. The mean value of the axial (\bar{U}) and radial velocities (\bar{V}) is calculated by averaging the velocity signals $u(t)$ and $v(t)$ as follows:

$$\bar{U} = \frac{1}{N} \sum_{i=1}^N u(t), \quad (5)$$

$$\bar{V} = \frac{1}{N} \sum_{i=1}^N v(t). \quad (6)$$

The data were collected for 16 s with a sampling frequency of 2^{16} Hz and were acquired at multiple points in the upstream domains, varying from $x/R = 0.27$ to 2 relative to the plane of rotation

(i.e., $x/R = 0$). Measurements were made on the x - y plane for an advance ratio of 0.52 at laminar, grid A and grid B inflows.

Figure 7 presents the contour maps of the normalized mean axial velocities (\bar{U}/U_∞), as measured from the hot-wire anemometer. The results compare the changes in the streamwise direction for the approaching laminar and grid turbulence inflows. The velocity vectors, which comprise the axial and radial velocity components, are presented on top of each contour to illustrate the change in the streamline's direction as it travels from the upstream position ($x/R = 2$) until just before it impinges on the blade's surface at ($x/R = 0$). For clarity, a shaded area of a single-blade propeller with radius R is added in the figure. The focus of the analysis has been put on the stagnation region in the immediate vicinity of the blade's surface, within one R distance away, where the flow acceleration is visible for all inflow conditions. The results show a localized area of axial flow acceleration along the middle sections of the blade, between $-0.3 < y/R < -0.8$.

On first inspection, one can observe increasing levels of flow acceleration in grid turbulence inflow cases compared to laminar. This phenomenon can be explained by the conventional propeller momentum theory, which implies that all fluids entering the streamtube of a propeller will be accelerated as it passes through the propeller disk due to the additional induced velocity component before exiting the streamtube far downstream.³⁰ The flow acceleration develops much earlier and with broader spatial extent in the upstream locations for grid B cases, at around $0.5R$ ahead of laminar and grid A inflow conditions. It has been observed that the grid turbulence cases demonstrate a slightly higher increase in the flow displacement of the approaching flow due to the distortion or elongation of turbulent vortical structures interacting within the accelerating streamtube. This phenomenon increases the possibility of fluctuating incident velocity impinging the blades and influences the potential effect of the oscillating pressure field along the surface of the blade, which agrees with the results of rms of velocity fluctuation shown in Fig. 9.

The distortion in the mean velocity magnitude within the acceleration zones may correspond to the artifact of the periodic aerodynamic interactions in the axial direction with respect to the azimuthal positions of the blade. The streamline curvature and streamtube contraction distort the upstream turbulence, causing the eddies in this domain to elongate and accelerate as they approach the propeller disk plane and "chopped" at the frequency of blade passing, resulting in periodicity effects in the velocity measurement. Such artifacts are not observed in the radial direction. The mean values of the radial velocity, as shown in Fig. 8, demonstrate continuous zones of radial velocity distribution between the midsection of the blade ($y/R = -0.5$) and slightly further from the tip, at around $y/R = -1.5$.

Regardless of the inflow conditions, Fig. 8 shows a significant increase in the distribution of the normalized mean radial velocity near the propeller tip as the flow approaches the near-stagnation region of the blade leading edge, between $x = 0.27R$ and $0.35R$. Within this domain, the mean velocity of the upward-moving airflow shows a relative increase compared to the freestream turbulence levels. The most significant increase occurs under grid B turbulence conditions, while the smallest increase is observed under the laminar inflow case. The flow within this domain is characterized by a strong deformation process, mainly due to the progressive bending of the blade wake surfaces. This distortion in the flow is induced by crossflow and the trajectory of the vortex generated at the propeller tip.³¹

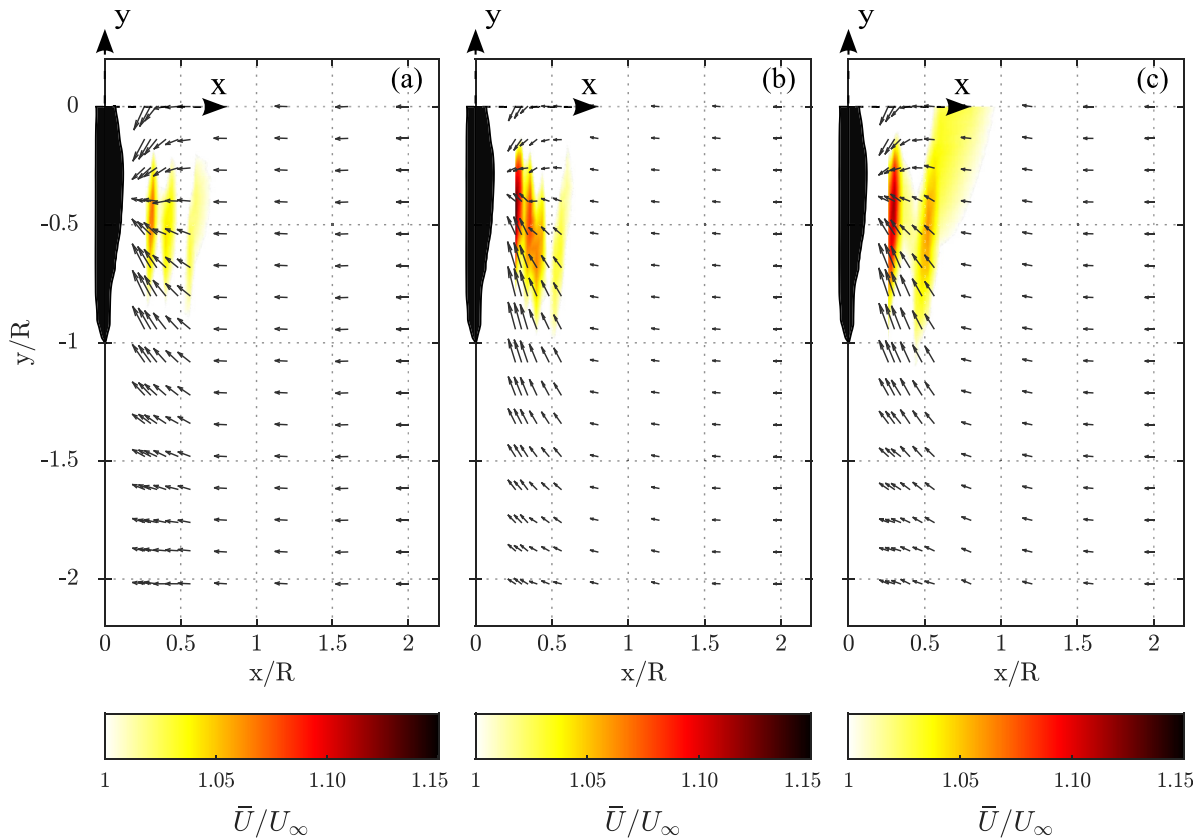


FIG. 7. The vector and contour map of the mean velocity in the axial direction for (a) laminar, (b) grid A, and (c) grid B inflow conditions.

The velocity fluctuations in the upstream field are calculated by decomposing the instantaneous velocity from the acquired hot-wire signals into a mean and fluctuating component; this helps to describe the characteristic of turbulent motion in the domain. The axial (u') and radial (v') velocity fluctuations in the upstream field are calculated by subtracting the mean velocity component from the velocity signals as follows:

$$u'(t) = u(t) - \bar{U}, \quad (7)$$

$$v'(t) = v(t) - \bar{V}. \quad (8)$$

The intensity of the turbulence fluctuations is expressed in terms of the root mean square of the velocity fluctuations, which have been calculated as follows:

$$U_{\text{rms}} = \sqrt{\frac{1}{N} \sum_{i=1}^N [u'(t)]^2}, \quad (9)$$

$$V_{\text{rms}} = \sqrt{\frac{1}{N} \sum_{i=1}^N [v'(t)]^2}. \quad (10)$$

The profiles of the calculated rms of axial velocity fluctuations (U_{rms}) in the upstream flow field domain are presented in Fig. 9.

The results are normalized with the freestream velocity (U_∞) and are depicted individually at 16 sequential axial positions to illustrate the evolution of the rms of velocity fluctuation as the airflow progresses toward the rotating propeller. At the most upstream locations, measured at approximately 80%–200% of blade radius distance away from the plane of rotation, deviations along the measurement axis (y -axis) are not visible for all three inflow conditions, as indicated in Figs. 9(m)–9(p). The mixing or transition region is identified to begin at $x/R = 0.59$, and as it gets closer to the propeller's blade surfaces, the magnitude of the fluctuation increases. The highest fluctuations occur around the midsection of the blade regardless of the inflow condition. However, the magnitude of the rms of velocity fluctuation varies with turbulence levels in the freestream. For instance, at $x/R = 0.27R$, the maximum fluctuation measured relative to the most upstream position increases by 7.5% in the case of laminar inflow, 8.3% in the case of grid A, and 9.4% in the case of grid B turbulence inflow.

Figure 10 presents the profiles of rms of radial velocity fluctuation (V_{rms}) normalized with the freestream velocity. For clarity, the measurement points in the upstream field domain are kept constant as previously discussed. Similar to the axial component, no visible deviations are observed along the y -axis for the rms of radial velocity fluctuations in the far upstream domain regardless of the inflow conditions. Notable changes in the trends begin at around $x/R = 0.59$. However, the results demonstrate a wave-like trend, with increasing and decreasing

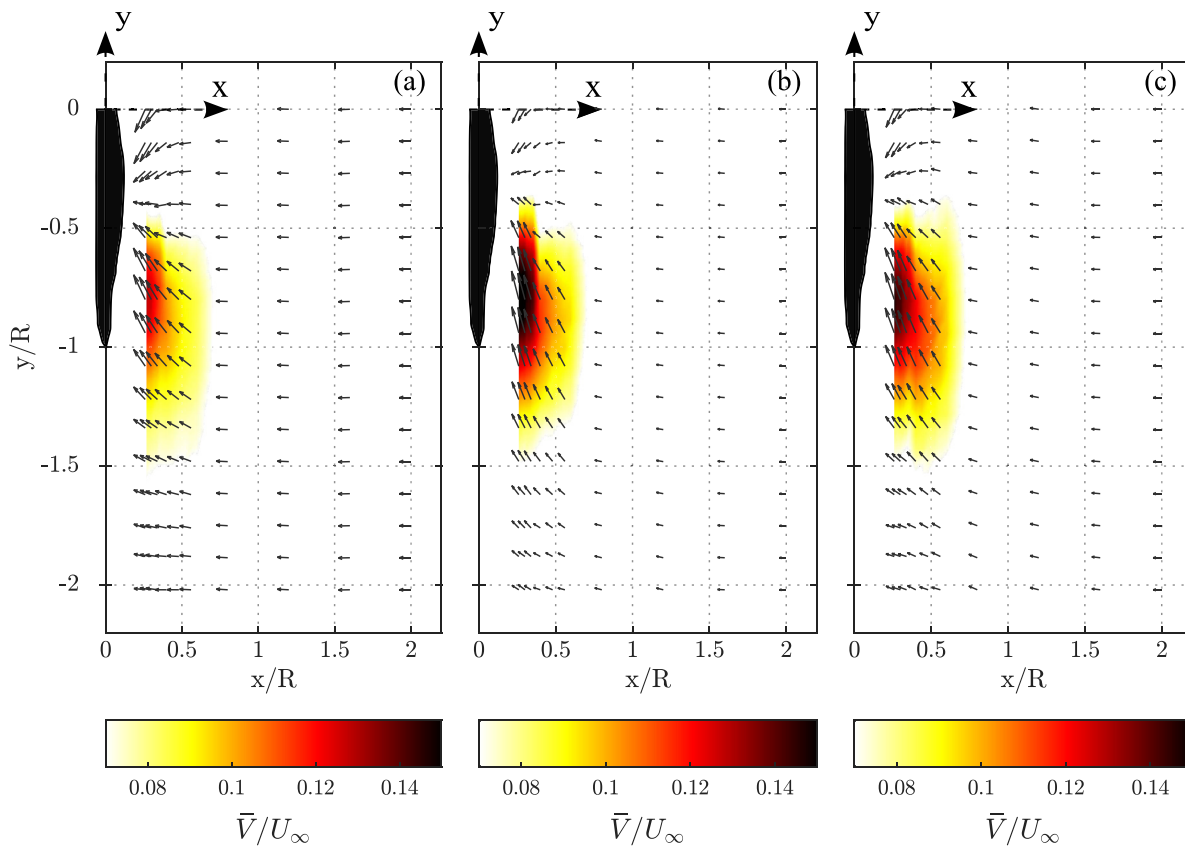


FIG. 8. The vector and contour map of the mean velocity in the radial direction for (a) laminar, (b) grid A, and (c) grid B inflow conditions.

fluctuations that vary along the blade radius. The largest fluctuations, indicated by the right-most points in the figures, are identified near the hub and the tip of the propeller, approximately at $y/R = 0$ and $y/R = -1$, respectively. The surge in the flow fluctuation near the propeller hub is due to the stagnation point at which high-velocity gradients and a wide-scale range of vortical structures are expected to occur. Meanwhile, the increase in rms of radial velocity fluctuations near the propeller's tip is attributed primarily to the vortical flow field within the domain, which induces the interactions with the blade tip vortices.

C. Energy spectrum of flow field

The energy content of the velocity fluctuations from CTA measurement was analyzed to understand its frequency response and how it changes in the upstream field. The data are presented in the form of power spectral density of the velocity fluctuations, estimated using Welch's method based on the time-domain data using Hamming windowing for segments of equal length with a 50% overlap. For brevity, results are presented along a radial position of $y/R = -0.8$, which is near the blade tip region, at four axial upstream locations, $x = 0.27R$, $0.43R$, $0.59R$, and $2.00R$. These locations represent the short domain in the immediate vicinity adjacent to the blade surfaces

and the most upstream field tested to highlight the changes that occur within the upstream flow field.

Figures 11(a)–11(d) depict the evolution in the energy spectra for axial velocity fluctuations (ϕ_{uu}), while the results for the radial velocity fluctuations (ϕ_{vv}) are presented in Figs. 11(e)–11(h). The overall spectra of the velocity fluctuation are characterized by its frequency-dependent content, especially the multiple peaks at the shedding frequency equivalent to the blade passage frequency (BPF) and its harmonics. BPF is calculated by multiplying the number of blades (b) and the rotational speed (n), $BPF = nb$. The peaks of these frequencies are not visible in the far upstream position but are most significant near the blade surfaces in Figs. 11(a) and 11(e) in both axial and radial directions, respectively. This characteristic is known as “haystacking,” a common acoustic feature caused by the aerodynamic interaction between the propeller blades and the ingested turbulent inflows. The results of this interaction produce broadband “haystackings” peaks in axial and radial velocity fluctuations. According to the literature, the peak frequency of those haystacks depends on the BPF, while the peak amplitude and the width should be related to the ingested turbulent structures.³² It is also well known that such a phenomenon is caused by the correlated unsteady loads when the consecutive blades ingest large-scale turbulence.³³ The peaks are commonly associated with the acoustic field and not the flow field. They are included to highlight the

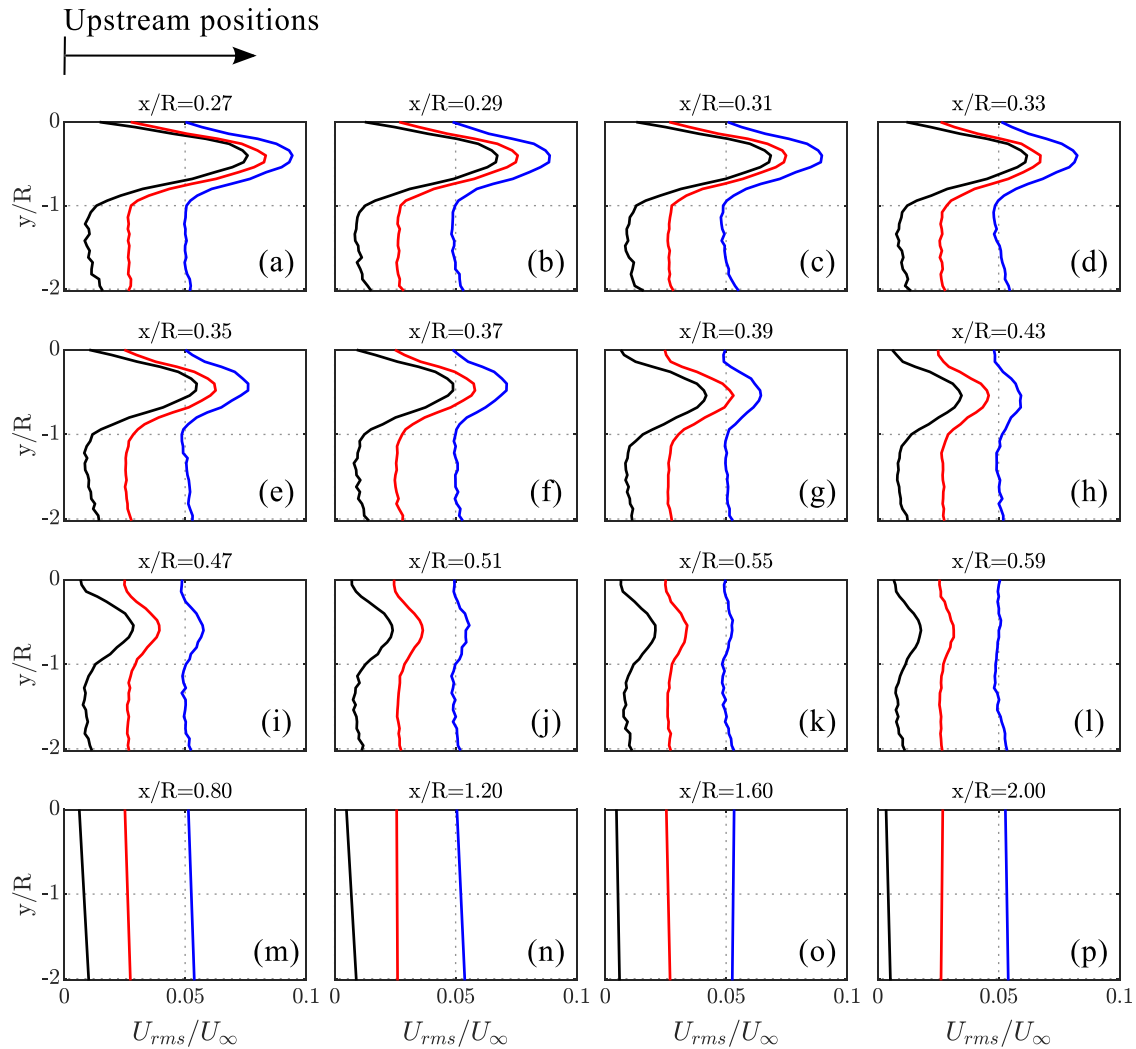


FIG. 9. Profiles of the normalized rms of axial velocity fluctuation in the upstream flow field for laminar (solid black line), grid A (solid red line), and grid B (solid blue line) at varying upstream positions: (a) $x = 0.27R$, (b) $x = 0.29R$, (c) $x = 0.31R$, (d) $x = 0.311R$, (e) $x = 0.35R$, (f) $x = 0.37R$, (g) $x = 0.39R$, (h) $x = 0.43R$, (i) $x = 0.47R$, (j) $x = 0.51R$, (k) $x = 0.55R$, (l) $x = 0.59R$, (m) $x = 0.80R$, (n) $x = 1.20R$, (o) $x = 1.60R$, and (p) $x = 2.00R$.

“haystack” peaks and will subsequently be filtered for the discussion of flow field data alone.

D. Far-field noise characteristics

Propeller noise radiated to the far-field is analyzed with respect to its directivity features and presented in terms of the overall sound pressure level (OASPL). The measurements of the OASPL are acquired by integrating the acoustic energy spectrum with respect to frequency using

$$OASPL = 10 \times \log_{10} \left[\frac{\int PSD(f) df}{P_{ref}^2} \right], \quad (11)$$

where PSD is the power spectral density of the sound pressure derived using Welch’s method based on the unsteady pressure fluctuation (p').³⁴

In the present work, the resolved frequency f is categorized into three ranges for the analysis of different noise components. The total noise OASPL considers a frequency range between 100 Hz and 30 kHz. Meanwhile, the low-frequency narrowband and high-frequency broadband OASPLs are resolved from 200 to 650 Hz and from 7 to 30 kHz, respectively.

Figure 12 depicts the total radiated OASPL for propeller rotating at advance ratios of 0.47, 0.66, and 0.85 in laminar and grid turbulent inflows. The results are presented across polar observation angles, ranging from the most upstream position ($\theta = 40^\circ$) to the farthest downstream ($\theta = 145^\circ$). Across all values of advance ratio presented, the results show maximum noise levels slightly downstream of the propeller, between $\theta = 100^\circ$ and 120° regardless of the inflow conditions. The upstream OASPL records an approximately 5–6 dB difference compared to the noise level recorded downstream at $J = 0.47$.

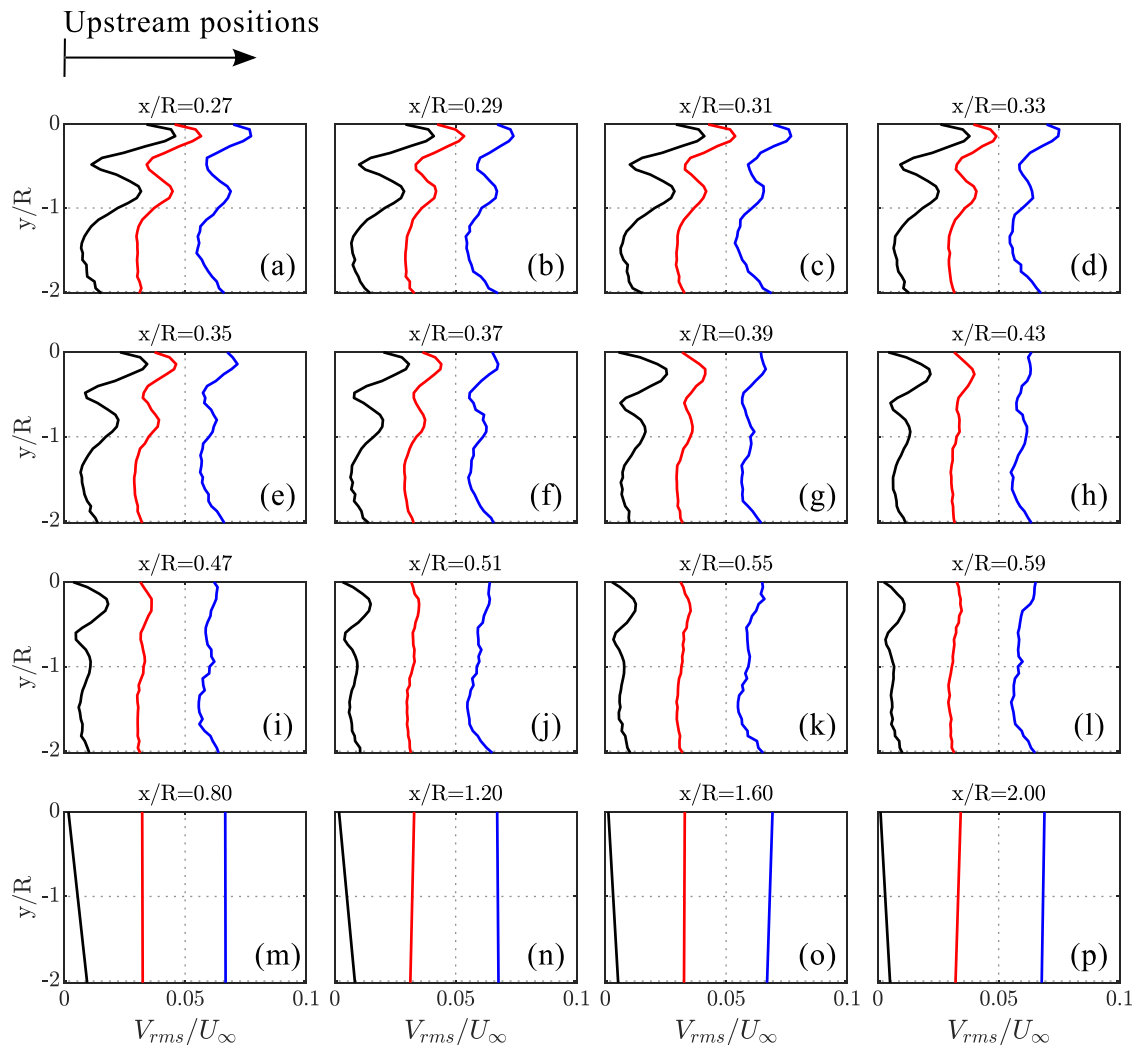


FIG. 10. Profiles of the normalized rms of radial velocity fluctuation in the upstream flow field for laminar (solid black line), grid A (solid red line), and grid B (solid blue line) at varying upstream positions: (a) $x = 0.27R$, (b) $x = 0.29R$, (c) $x = 0.31R$, (d) $x = 0.311R$, (e) $x = 0.35R$, (f) $x = 0.37R$, (g) $x = 0.39R$, (h) $x = 0.43R$, (i) $x = 0.47R$, (j) $x = 0.51R$, (k) $x = 0.55R$, (l) $x = 0.59R$, (m) $x = 0.80R$, (n) $x = 1.20R$, (o) $x = 1.60R$, and (p) $x = 2.00R$.

This discrepancy reduces at higher advance ratios as the amplitude of OASPL amplifies across all polar observation angles in the field. Additionally, the ingestion of grid turbulence leads to an increase in the OASPL relative to the laminar inflow in both upstream and downstream locations. On a closer look at the results, the OASPL for the grid B case is slightly more dominating than grid A at lower advance ratios and is relatively equivalent at larger advance ratios.

The radiation patterns resemble a cardioid-shaped directivity with its dipole axis aligned to the propeller’s rotation axis at the lower range advance ratio and slightly skewed to the plane of rotation at a higher advance ratio. The former suggests a strong presence of loading noise components in the overall spectrum, while the latter is due to the dominating broadband acoustics response at higher inflow speed. These findings indicate a maximum pressure perturbation in the plane of rotation that may be contributed by the acoustic sources that are

tonal in nature, including the rotation of steady blade loading at harmonics of BPF.³⁵ Deepak *et al.* also observe a similar trend, which infers that tonal noise is most dominant at low tip Mach number operation, especially for low blade propellers.³⁶ It has also been previously observed that the acoustic waves generated by the aerodynamic loading diffract at the blade trailing edge, forming a dipole-like acoustic source with cardioid directivity oriented toward the plane of rotation.³⁷

The directivity and intensity of different noise components are extracted from the same OASPL data and demonstrated in the form of BPF tone and broadband sound levels in Fig. 13. The analysis decomposes the overall sound spectrum and represents them in the form of acoustic energy contained in the blade passage frequency and the high-frequency domains. Regardless of the inflow conditions and velocity, the tonal noise at BPF presents a similar directivity feature as

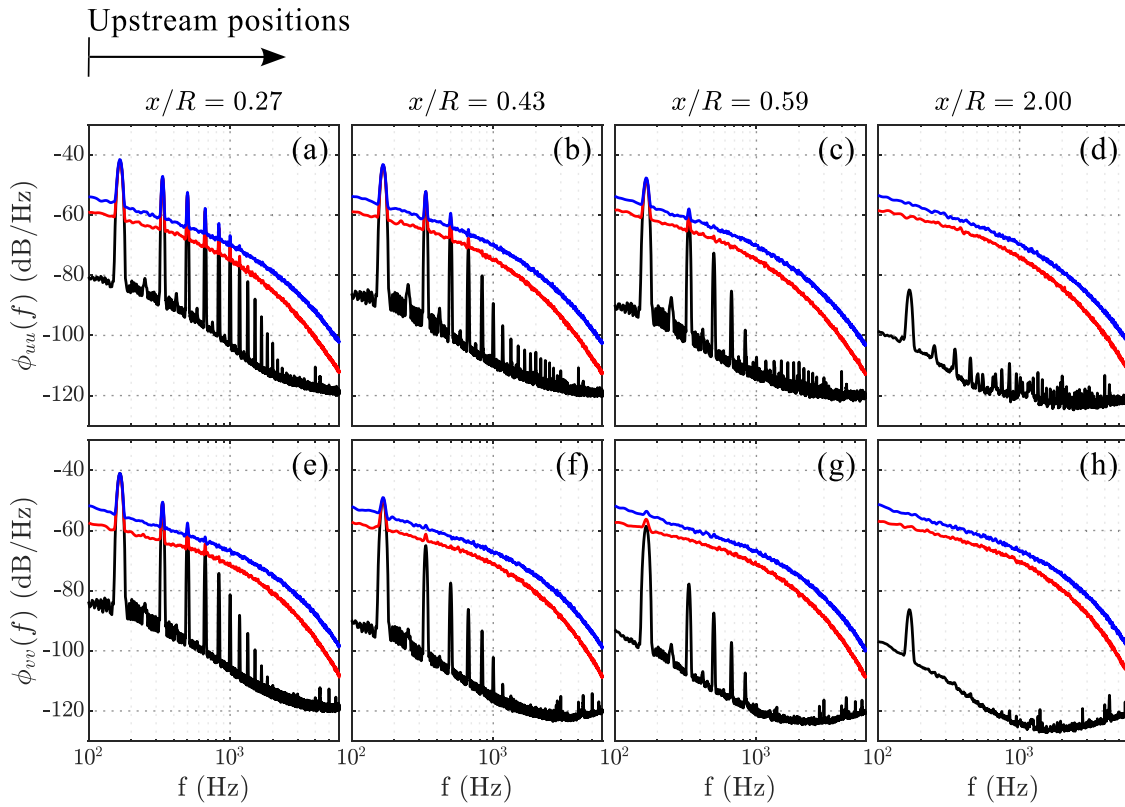


FIG. 11. PSD of axial [(a)–(d)] and radial velocity fluctuations [(e)–(h)] for the laminar (solid black line), grid A (solid red line), and grid B inflow cases (solid blue line) computed from the hot-wire measurements at an advance ratio operation of 0.5 near the tip of the propeller.

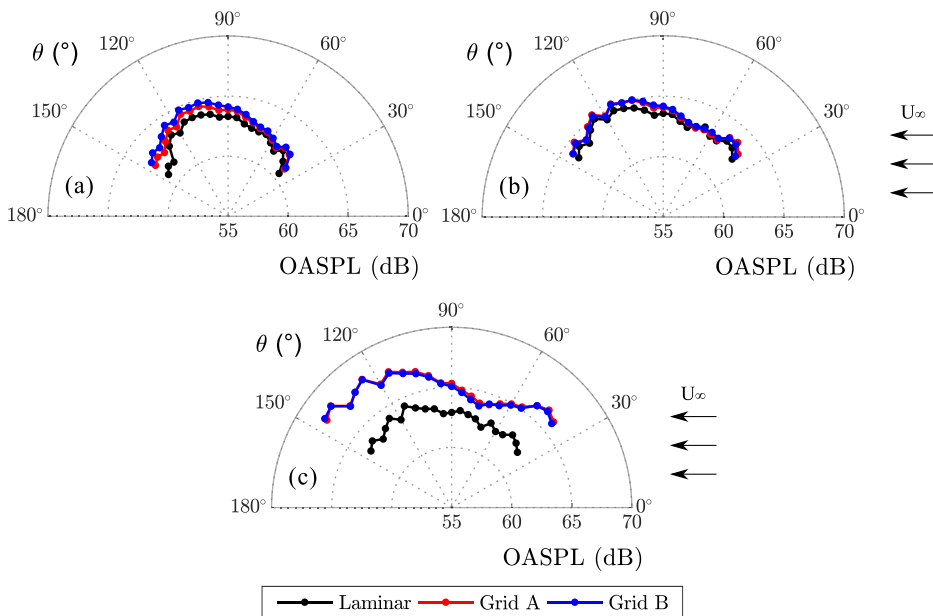


FIG. 12. Directivity and intensity of OASPL at an advance ratio of (a) 0.47, (b) 0.66, and (c) 0.85.

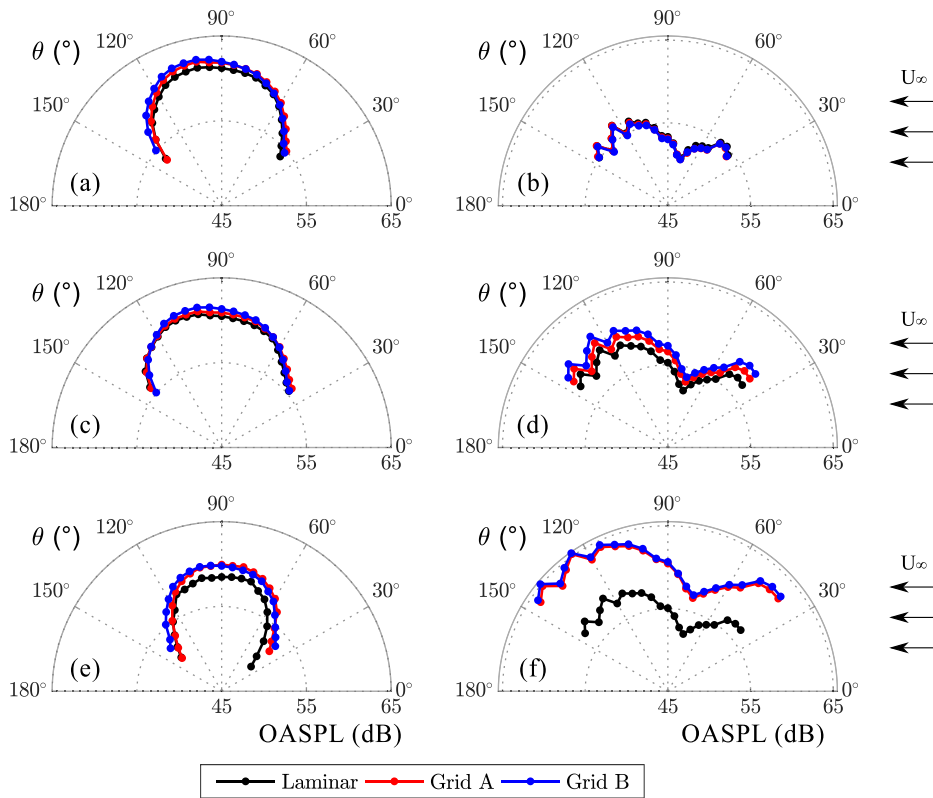


FIG. 13. Comparisons of the directivity features of the BPF tone [(a), (c), and (e)] and the broadband noise component [(b), (d), and (f)] in laminar and grid turbulence inflows at a 0.5 advance ratio operation.

the overall noise where the maximum levels are oriented along the plane of rotation. On the other hand, the maximum broadband noise’s directivities are oriented toward the rotational axis and have a relatively low intensity near the plane of rotation and maximum away from it. The broadband contribution is more prominent than the BPF tone at higher advance ratio operations, and the effect increases with turbulence ingestion, which agrees with the OASPL trend.

The power spectrum of acoustic pressure fluctuations was estimated using Welch’s method,³⁴ where the data were segmented for 32 equal lengths with a 90% overlap and windowed using the Hamming function, resulting in a spectral frequency resolution of $\delta f = 1$ Hz. The data obtained yields an absolute uncertainty of ± 0.05 dB with a 95% confidence level. Results are presented in terms of sound pressure level (SPL) spectra, which are calculated as follows:

$$SPL = 20 \log_{10} \frac{p_{rms}}{p_{ref}}, \quad (12)$$

where p_{rms} in the equation refers to the root mean square of the measured acoustic pressure, and p_{ref} is the conventional reference pressure of $20 \mu\text{Pa}$. Figure 14 presents the comparison of SPL spectra of an isolated propeller as a function of inflow conditions and advance ratio. The presented results were extracted at an observation location of $\theta = 90^\circ$ relative to the upstream direction, as illustrated in the test setup schematic in Fig. 2. The results are presented in three separate frequency domains, representing the total noise spectra, the BPF tonal noise, and the high-frequency broadband noise. Results are obtained for a constant rotational speed at three different advance ratios of 0.47,

0.66, and 0.85, presented from top to bottom of the figure. The noise spectra are also compared with the unloaded motor and background noise at a given rotation speed, demonstrating minimum contamination from the motor. It is worth noting that the discrete tone in the mid- and high-frequency ranges (2500 Hz–10 kHz) may be potentially associated with the motor or electronic speed controller.

Across all tested parameters, the propeller noise spectra consistently demonstrated a high content of narrowband tonal noise at discrete frequencies and a widely distributed broadband noise over the entire frequency domain. High amplitude peaks at the BPF and its harmonics can be observed in the lower frequency domain, similar to the haystacking trends seen at the PSD of velocity fluctuation. However, the total numbers of the peaks are different between these PSDs. The tonal noise spectra at BPF are shown in Figs. 14(b), 14(e), and 14(g), where high-amplitude discrete tones are detected in all measured flow conditions. The magnitude of the BPF tonal peaks increases in grid cases compared to laminar inflow. This trend is expected, implying that grid turbulence ingestion influences blade tonal noise levels due to the increase in blade loading, as previously described.

In the literature, each blade section of a propeller may experience a variation in its broadband acoustic response within one blade rotation. It may also vary with the aerodynamic interactions with the ingested turbulence.¹³ The experimental results demonstrate such a variation in the high-frequency domain, as depicted in Figs. 14(c), 14(f), and 14(h), where the broadband noise is presented in terms of the non-dimensional Helmholtz number (kc), calculated as $kc = \omega_o c / c_o$, where ω_o is the

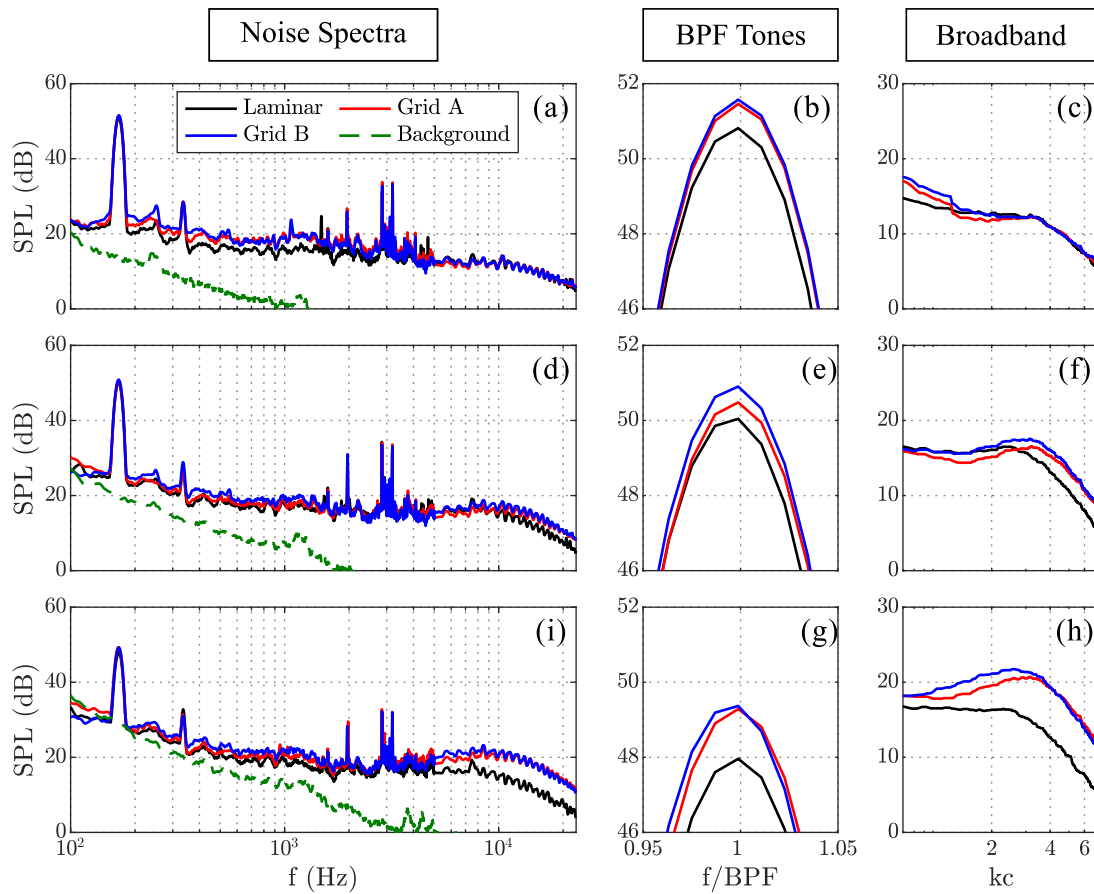


FIG. 14. Sound pressure level spectra for propeller in laminar and grid turbulence inflows presented in the total frequency domain, narrowband blade passage frequency, and high-frequency domain in terms of the non-dimensional Helmholtz number (kc). Subplots (a)–(c) represent the results for an advance ratio of $J = 0.47$, (d)–(f) for $J = 0.66$, and (i)–(h) for $J = 0.85$ at a constant rotational speed of 5000 rpm.

source frequency, c_0 is the speed of sound, and c is the propeller chord length at a 75% radius. The broadband noise humps are evident in the mid- and high-frequency ranges of the spectra, between 2.5 and 10 kHz. This phenomenon is believed to be due to turbulence ingestion, as the existence of turbulence structures in the approaching grid-turbulent flow increases the temporal variation of the inertia of vortices, speeding up the distortion and finally leading to a more efficient conversion of vortical energy to sound. This feature may also be associated with blade self-noise, i.e., interaction of the blade with its boundary layer or tip flow in the case of laminar flow. However, further investigation is required to analyze this noise-generating mechanism.

Based on the OASPL radiation directivities, the spectral analysis was conducted at both upstream and downstream observation positions. The energy-frequency content of the radiated noise was examined at $\theta = 60^\circ$ for upstream noise radiation and at $\theta = 120^\circ$ for downstream, in comparison to the baseline spectra measured at the plane of rotation at $\theta = 90^\circ$. Figure 15 presents the comparison of acoustic spectra for propeller operating at a constant rotational speed of 5000 rpm and $J = 0.85$ at different observation positions.

The noise spectra at both upstream and downstream positions, as shown in Figs. 15(a) and 15(c), show only marginal differences in BPF tonal peak amplitudes by approximately 1–3 dB compared to the spectra at the plane of rotation. However, significant variation in the broadband noise components is observed, especially within the low-to-mid range of frequency, between 200 and 2000 Hz. This trend indicates a more dominant contribution of broadband noise outside the plane of rotation compared to the tonal noise. There is also a noticeable increase in high-frequency broadband noise at the downstream observation position. This observation further suggests a more intense radiation of broadband noise out of the rotation plane in the wake of the propeller under forward flight conditions.

IV. CONCLUSION

In this work, the effects of turbulence ingestion on the aerodynamic noise of a propeller were investigated under forward flight configuration with laminar and grid turbulence inflow conditions. The far-field noise spectral characteristics of the propeller were characterized by distinct tones and broadband noise components. The results demonstrated a substantial influence on the discrete tonal noise in the

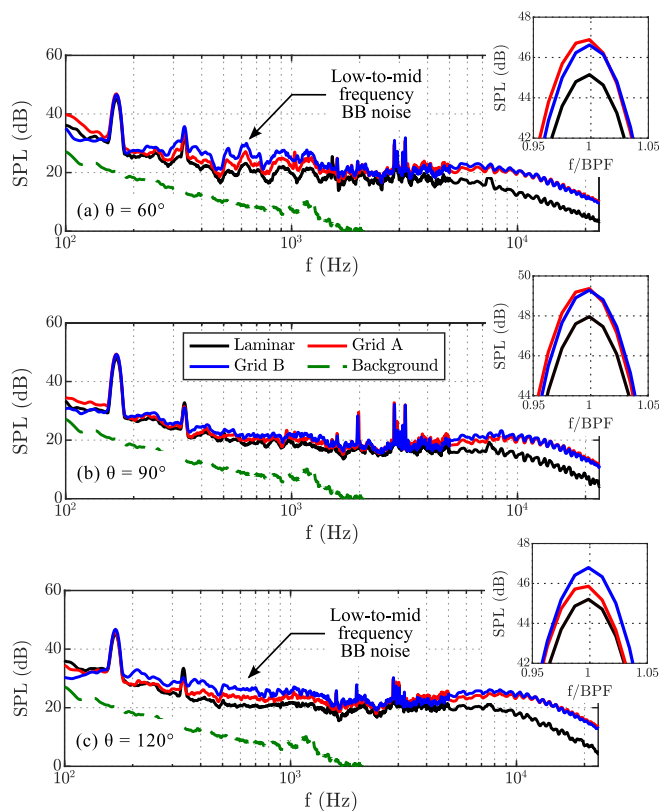


FIG. 15. Comparison of the acoustic spectra for propeller in laminar and grid turbulence inflows at an observation position of (a) $\theta = 60^\circ$, (b) $\theta = 90^\circ$, and (c) $\theta = 120^\circ$ under a constant rotational operation of 5000 rpm and $J = 0.85$.

fundamentals and harmonics of blade passing frequencies and the broadband noise response. These characteristics suggest that the low-frequency narrowband and high-frequency broadband noise content are strongly influenced by turbulence ingestions, causing variation in both noise levels and radiation patterns of the propeller's acoustics response. The results indicate that at a frequency band above 1000 Hz, the noise spectra increase by about 2 dB/Hz for grid A cases and around 5 dB/Hz for grid B cases relative to the baseline laminar inflow cases. The observed trends in the noise spectra and directivity show that the tonal noise radiation is predominantly directed toward the plane of rotation, while the broadband noise radiation is predominantly directed outside the plane of rotation. The directivity behavior of the overall sound pressure level suggests that maximum radiation occurs over the plane of rotation and exhibits a slightly skewed downstream orientation, with higher inflow velocity and turbulence ingestion. The flow analysis of the approaching field reveals a haystacking feature in the frequency-energy content of the fluctuating velocities in axial and radial directions, similar to the trends seen in the far-field sound pressure levels. The examination of the propeller's aerodynamic force suggests that turbulence ingestion increases generated thrust due to the increase in pressure by the propeller blade to compensate for the drop of pressure induced by the incoming grid turbulence. These trends are observed from the increasing magnitude of the mean

velocities in the axial and radial directions within a small domain in the upstream flow field adjacent to the propeller blade surfaces. Overall, the grid B inflow has the largest tested length scale of turbulence structures and records the highest variation of the aerodynamic performance, the mean and fluctuating inflow velocities, and the noise levels compared to the clean-laminar inflows.

ACKNOWLEDGMENTS

The first author would like to acknowledge the financial support of Majlis Amanah Rakyat Malaysia. The second author would like to acknowledge the EPSRC (Engineering and Physical Sciences Research Council) for post-doctoral sponsorship at the University of Bristol from June 2020 to December 2021 (Grant No. EP/S013024/1). The first and third authors would like to acknowledge Horizon 2020 research and innovation programme under Grant Agreement No. 882842 (SilentProp project). All authors would like to thank Luke Bowen for his assistance in manufacturing and analyzing the grid.

AUTHOR DECLARATIONS

Conflict of Interest

The authors have no conflicts to disclose.

Author Contributions

Nur Syafiqah Jamaluddin: conceptualization (equal); data curation (equal); formal analysis (equal); investigation (equal); methodology (equal); project administration (equal); resources (equal); software (equal); validation (equal); visualization (equal); writing—original draft (equal); and writing—review and editing (equal). **Alper Celik:** data curation (supporting); formal analysis (equal); investigation (supporting); methodology (supporting); software (supporting); validation (supporting); visualization (equal); and writing—review and editing (equal). **Kabilan Baskaran:** data curation (equal); formal analysis (equal); investigation (equal); software (equal); validation (equal); and writing—review and editing (equal). **Djamel Rezgui:** conceptualization (supporting); formal analysis (supporting); funding acquisition (lead); project administration (equal); resources (lead); supervision (lead); and writing—review and editing (equal). **Mahdi Azarpeyvand:** conceptualization (supporting); formal analysis (supporting); funding acquisition (lead); project administration (equal); resources (lead); supervision (lead); and writing—review and editing (equal).

DATA AVAILABILITY

The data that support the findings of this study are available within the article.

REFERENCES

- ¹A. Filippone and G. N. Barakos, "Rotorcraft systems for urban air mobility: A reality check," *Aeronaut. J.* **125**, 3–21 (2021).
- ²See <https://evtol.news/aircraft> for information related to various eVTOL aircraft designs.
- ³K. R. Antcliff, S. K. Whiteside, L. W. Kohlman, and C. Silva, "Baseline assumptions and future research areas for urban air mobility vehicles," AIAA Paper No. 2019-0528, 2019.
- ⁴D. Kurtz and J. Marte, "A review of aerodynamic noise from propellers, rotors, and lift fans," Technical Report No. 32-1462 (NASA Jet Propulsion Laboratory, Pasadena, CA, 1970).

- ⁵K. Baskaran, A. Celik, N. S. Jamaluddin, D. Rezgui, and M. Azarpeyvand, "Aerodynamic and aeroacoustic characteristics of different pitch propellers," AIAA Paper No. AIAA 2022-3107, 2022.
- ⁶K. Baskaran, N. S. Jamaluddin, A. Celik, D. Rezgui, and M. Azarpeyvand, "Aerodynamic and aeroacoustic characteristics of propellers with different blade numbers," AIAA Paper No. AIAA 2022-3108, 2022.
- ⁷E. Grande, G. Romani, D. Ragni, F. Avallone, and D. Casalino, "Aeroacoustic investigation of a propeller operating at low Reynolds numbers," *AIAA J.* **60**, 860 (2022).
- ⁸N. A. Pettingill, N. S. Zawodny, C. Thurman, and L. V. Lopes, "Acoustic and performance characteristics of an ideally twisted rotor in hover," AIAA Paper No. AIAA 2021-1928, 2021.
- ⁹S. Meloni, E. de Paola, E. Grande, D. Ragni, L. G. Stoica, A. D. Marco, and R. Camussi, "A wavelet-based separation method for tonal and broadband components of low Reynolds-number propeller noise," *Meas. Sci. Technol.* **34**, 044007 (2023).
- ¹⁰W. Chen, B. Peng, R. P. Liem, and X. Huang, "Experimental study of airfoil-rotor interaction noise by wavelet beamforming," *J. Acoust. Soc. Am.* **147**, 3248–3259 (2020).
- ¹¹Y. Yang, Y. Liu, H. Hu, X. Liu, Y. Wang, E. Arcondoulis, and Z. Li, "Experimental study on noise reduction of a wavy multi-copter rotor," *Appl. Acoust.* **165**, 107311 (2020).
- ¹²L. Marino, "Experimental analysis of UAV propeller noise," AIAA Paper No. AIAA 2010-3854, 2010.
- ¹³Z. F. Gan, K. S. Brentner, and E. Greenwood, "Time variation of helicopter rotor broadband noise," AIAA Paper No. AIAA 2914-2022, 2022.
- ¹⁴H. Jiang, H. Wu, W. Chen, P. Zhou, S. Zhong, X. Zhang, G. Zhou, and B. Chen, "Toward high-efficiency low-noise propellers: A numerical and experimental study," *Phys. Fluids* **34**, 076116 (2022).
- ¹⁵H. Wu, W. Chen, H. Jiang, S. Zhong, and X. Zhang, "Experimental investigation of the effect of sectional airfoil profile deviation on propeller noise," *Phys. Fluids* **35**, 027104 (2023).
- ¹⁶N. S. Jamaluddin, A. Celik, K. Baskaran, D. Rezgui, and M. Azarpeyvand, "Aeroacoustic performance of propellers in turbulent flow," AIAA Paper No. AIAA 2021-2188, 2021.
- ¹⁷J. M. Anderson, M. R. Catlett, and D. Stewart, "Modeling rotor unsteady forces and sound due to ingestion of spatially inhomogeneous turbulence," AIAA Paper No. AIAA 2014-2607, 2014.
- ¹⁸H. H. Hubbard, "Aeroacoustics of flight vehicles: Theory and practice. Volume 1: Noise sources," Technical Report No. 90-3052 (National Aeronautics and Space Administration Langley Research Center NASA Langley Research Center, Hampton, VA, 1991).
- ¹⁹R. A. V. Robison and N. Peake, "Noise generation by turbulence-propeller interaction in asymmetric flow," *J. Fluid Mech.* **758**, 121–149 (2014).
- ²⁰D. F. Scharpf and T. J. Mueller, "An experimental investigation of the sources of propeller noise due to the ingestion of turbulence at low speeds," *Exp. Fluids* **18**, 277–287 (1995).
- ²¹M. Sevik, "Sound radiation from a subsonic rotor subjected to turbulence," in *Fluid Mechanics, Acoustics, and Design of Turbomachinery Part II* (National Aeronautics and Space Administration, Washington, DC, 1974) Vol. 304, pp. 493–511.
- ²²J. P. Wojno, T. J. Mueller, and W. K. Blake, "Turbulence ingestion noise, Part 1: Experimental characterization of grid-generated turbulence," *AIAA J.* **40**, 16–25 (2002).
- ²³J. P. Wojno, T. J. Mueller, and W. K. Blake, "Turbulence ingestion noise, Part 2: Rotor aeroacoustic response to grid-generated turbulence," *AIAA J.* **40**, 26–32 (2002).
- ²⁴J. Wu, J. Yangzhou, Z. Ma, and X. Huang, "Numerical study of rotor unsteady forces and noise due to ingestion of grid-generated turbulence," *Phys. Fluids* **35**, 015141 (2023).
- ²⁵Y. Mayer, H. K. Jawahar, M. Szoke, and M. Azarpeyvand, "Design of an aeroacoustic wind tunnel facility at the University of Bristol," in 24th AIAA/CEAS Aeroacoustics Conference, 2018.
- ²⁶F. E. Jørgensen, *How to Measure Turbulence with Hot-Wire Anemometers: A Practical Guide* (Dantec Dynamics, 2002).
- ²⁷See <https://www.apcprop.com/technical-information/engineering> for technical information and resources related to the engineering aspects of Advanced Precision Composites (APC) propellers.
- ²⁸L. Bowen, A. Celik, M. Azarpeyvand, and C. R. I. da Silva, "Grid generated turbulence for aeroacoustic facility," *AIAA J.* **60**, 1833–1815 (2022).
- ²⁹J. Dominique, F. Ailloud, O. Cheriaux, M. Henner, J. Christophe, and C. Schram, "The impact of distorted inflow on a centrifugal fan noise," in *International Conference on Fan Noise, Aerodynamics, Applications and Systems* (Technische Universität Darmstadt, 2022), p. 10.
- ³⁰W. F. Phillips, "Propeller momentum theory with slipstream rotation," *J. Aircr.* **39**, 184–187 (2002).
- ³¹A. Stella, G. Guj, and F. D. Felice, "Propeller wake flowfield analysis by means of LDV phase sampling techniques," *Exp. Fluids* **28**, 1–10 (2000).
- ³²Z. Xiong, W. Rui, L. Lu, G. Zhang, and X. Huang, "Experimental investigation of broadband thrust and loading noise from pumpjet due to turbulence ingestion," *Ocean Eng.* **255**, 111408 (2022).
- ³³W. N. Alexander, W. J. Devenport, and S. A. Glegg, "Noise from a rotor ingesting a thick boundary layer and relation to measurements of ingested turbulence," *J. Sound Vib.* **409**, 227–240 (2017).
- ³⁴W. Liu, J. A. Zagzebski, and W. Liu, "Trade-offs in data acquisition and processing parameters for backscatter and scatterer size estimations," *IEEE Trans. Ultrason., Ferroelectr., Freq. Control* **57**, 340–352 (2010).
- ³⁵E. Greenwood, K. S. Brentner, R. F. Rau II, and Z. F. T. Gan, "Challenges and opportunities for low noise electric aircraft," *Int. J. Aeroacoustics* **21**, 315–367 (2022).
- ³⁶D. C. Akiwate, A. B. Parry, P. Joseph, and C. C. Paruchuri, "On the balance between the tonal and broadband noise of uninstalled propellers," AIAA Paper 2021-2308, 2021.
- ³⁷A. Filippone, "Aircraft noise prediction," *Prog. Aerosp. Sci.* **68**, 27–63 (2014).